Remediation Ecology
https://www.sciltp.com/journals/re

Article

Active Treatment of Oily Emulsion Wastewater by Bio-Derived Tubular Micromotors

Ziming Wang, Mengyin Tan and Hong Wang *

School of Chemical Engineering & Technology, China University of Mining and Technology, Xuzhou 221116, China
* Correspondence: hongwang@cumt.edu.cn

How To Cite: Wang, Z.; Tan, M.; Wang, H. Active Treatment of Oily Emulsion Wastewater by Bio-Derived Tubular Micromotors. *Remediation Ecology* **2026**, *1*(1), 5.

Received: 3 June 2026
Revised: 2 July 2026
Accepted: 4 August 2026
Published: 11 August 2026

Abstract: The treatment of oil-in-water emulsion wastewater remains a challenge due to the presence of finely dispersed oil droplets stabilized by surfactants. Herein, an active demulsifier based on the bio-templated tubular micromotor was designed. The hollow architecture of naturally abundant kapok fibers facilitates generation of micro/nanobubbles catalyzed by MnO_2 immobilized on the surface and enables efficient propulsion of the tubular structure in H_2O_2 solution, while the integrated Fe_3O_4 nanoparticles endow the micromotors with facile magnetic recyclability. To enhance interaction with oil droplets, a polydopamine interlayer is introduced for subsequent fluorinated thiol grafting. The tailored surface properties of micromotors together with the bubble-driven propulsion greatly facilitated the demulsification process. Comparison between the static control experiments and the self-propelled micromotors corroborated the contribution of bubble propulsion. Under optimized conditions, a demulsification efficiency of 98.19% was achieved within 27 min, markedly superior to that obtained in the static system. The self-propelled micromotors effectively accelerated emulsion destabilization through autonomous locomotion and bubble-assisted flotation effects. This proposed micromotor provides a promising platform for the remediation of emulsified oily wastewater.

Keywords: micromotors; demulsifier; oil-water separation; kapok fiber; surface modification

1. Introduction

Oily wastewater generated from industrial activities and marine transportation has become a pressing environmental concern worldwide [1]. Large volumes of oily effluents are produced by various sectors, including the petrochemical [2], textile [3], food-processing [4], and shipping industries [5], and also originate from crude oil spills and the discharge of oily bilge water during maritime operations [6,7]. These contaminants pose serious threats to aquatic ecosystems, water resource safety, and ecological sustainability [8,9]. In particular, oil-in-water emulsions containing finely dispersed oil droplets stabilized by surfactants are highly resistant to conventional separation processes, making their treatment a major challenge in wastewater remediation [10]. Oily contaminants in wastewater generally exist as free oil, dispersed oil, and emulsified oil [11]. These three forms require different separation strategies depending on droplet size and interfacial stability [12,13]. Conventional oil-water separation technologies, such as gravity separation, dissolved air flotation, and centrifugation, are often ineffective for treating stable oil-in-water emulsions and are associated with high energy consumption, limited separation efficiency, and secondary waste generation [14,15]. Among existing feasible technologies, membrane filtration has attracted considerable attention due to its high separation efficiency and operational simplicity [16,17]. However, membrane-based processes are constrained by membrane fouling, high operational costs, and the need of pretreatment to mitigate scaling and clogging [18]. Therefore, developing efficient and sustainable demulsification technologies for stable emulsified oily wastewater remains an urgent need.

Recently, self-propelled micro/nanomotors have emerged as a promising platform for treating emulsified oily wastewater owing to their autonomous motion and enhanced interfacial mass transfer [19–21]. Unlike conventional static separation materials, micro/nanomotors can actively interact with dispersed oil droplets, thereby increasing contact frequency and accelerating demulsification processes. Previous studies have shown that bubble-propelled micromotors with hydrophobic surfaces can efficiently capture oil droplets and promote oil-water separation [22,23]. In particular, bio-derived micromotors based on natural materials such as plant pollen have demonstrated considerable potential due to their surface functionality and renewable nature [24]. Despite these advances, the practical applications of micro/nanomotors remain limited by challenges including complex fabrication procedures, insufficient recyclability, and limited environmental compatibility [25,26]. Hence, developing low-cost, recyclable, and bio-derived micromotors with efficient demulsification capability may offer new possibilities for the treatment of emulsion wastewater.

Bio-derived materials have attracted increasing attention in oil pollution remediation because of their abundant reserves, low production cost, and excellent biocompatibility [27–29]. Kapok fiber (KF) is a natural tubular fiber obtained from the seed pods of the kapok tree. It is recognized as the natural hollow fiber with the lowest known density, featuring an ultrathin wall (approximately 0.8–1.0 μm), an outer diameter of 15–25 μm, and a hollow ratio of up to 97% [30]. Owing to its unique hollow tubular structure and low density, kapok fiber exhibits excellent oil affinity, high liquid retention capacity, and efficient adsorption of oil films on water surfaces through capillary action, making it a promising natural material for oil-water separation applications [31]. However, the surface of raw kapok fibers is covered by a natural wax layer, which limits further surface functionalization and hinders the effective utilization of the internal hollow structure for liquid storage. Therefore, in order to construct micromotor platforms based on kapok fibers for efficient oil-water separation, appropriate surface treatment and functional modification are essential.

In this study, kapok fibers were employed as bio-derived tubular templates to construct a self-propelled micromotor demulsifier for the treatment of emulsified oily wastewater. Fe_3O_4 and MnO_2 nanoparticles were sequentially deposited onto the fiber surface through co-deposition and impregnation processes, endowing the micromotors with magnetic responsiveness and catalytic bubble-driven propulsion. Subsequently, a functional polydopamine (PDA) interlayer was introduced via dopamine oxidative self-polymerization, followed by hydrophobic modification through the covalent grafting of 1H,1H,2H,2H-perfluorodecanethiol onto the active groups of polydopamine. The effectiveness of the surface modification was evaluated by analyzing changes in surface energy and wettability before and after functionalization. In addition, the contribution of autonomous micromotor motion to demulsification performance was investigated through static and self-propelled comparative experiments. Key operational parameters, including pH, micromotor dosage, and reaction temperature, were optimized to maximize demulsification efficiency. The resulting bio-derived micromotor demulsifier achieved rapid and efficient demulsification of emulsified oily wastewater, providing a promising strategy for oily wastewater treatment.

2. Experimental Section

2.1. Materials and Apparatus

Detailed information of materials and related characterization apparatus was recorded in Text S1.

2.2. Preparation of FPMs

Kapok fibers were first cut into short segments and used as the substrate for Fe_3O_4 deposition via a coprecipitation process. Typically, 0.2 g of kapok fibers was dispersed in 100 mL of deionized water and ultrasonicated for 30 min to remove dissolved oxygen. Subsequently, $FeCl_3 \cdot 6H_2O$ (0.94 g) and $FeCl_2 \cdot 4H_2O$ (0.36 g) were added and stirred for 30 min. Ammonia solution was then added dropwise until the pH was about 10, followed by heating at 70 °C for 30 min. The obtained Fe_3O_4-coated kapok fibers were magnetically separated, washed thoroughly with deionized water and ethanol, and freeze-dried. The resulting product was denoted as Fe_3O_4@KF.

MnO_2 was subsequently loaded onto Fe_3O_4@KF through $KMnO_4$ impregnation. Specifically, 0.5 g of Fe_3O_4@KF and 5.0 g of $KMnO_4$ were dispersed in 30 mL of deionized water and soaked for 24 h. The resulting product was magnetically collected, washed with deionized water and ethanol, and freeze-dried to obtain MnO_2@Fe_3O_4@KF.

For polydopamine functionalization, 0.2 g of MnO_2@Fe_3O_4@KF and 0.2 g of dopamine hydrochloride were dispersed in 100 mL of Tris buffer (10 mM, pH 8.5). The suspension was shaken for 24 h under ambient aerobic conditions to allow the oxidative self-polymerization of dopamine on the fiber surface. The PDA-coated product

was magnetically separated, washed with deionized water and ethanol, and freeze-dried. The obtained material was denoted as PDA@MnO_2@Fe_3O_4@KF.

To obtain hydrophobic micromotors, 0.1 g of PDA@MnO_2@Fe_3O_4@KF was dispersed in 30 mL of ethanol, followed by the addition of 0.3 mL of 1H,1H,2H,2H-perfluorodecanethiol and 100 μL of triethylamine. After reaction at room temperature for 24 h, the product was collected by centrifugation, washed three times with n-hexane, and dried to obtain fluorinated PDA-functionalized micromotors (FPMs).

2.3. Preparation of Oil-in-Water Emulsion

5.0 g of dimethyl silicone oil was precisely weighed into a 100 mL beaker. 2.0 mL 1.0 M NaCl solution, 4.0 mL n-pentanol, and 0.4 g Tween 80 were added sequentially. Deionized water was supplemented to reach a total mass of 100.0 g. The mixture was equilibrated in a constant-temperature water bath (40 °C) for 3 min, then emulsified in a high-pressure homogenizer (7000 rpm) for 10 min to obtain a stable oil-in-water emulsion.

2.4. Motion Study of Micromotors

The motion behaviors of chemically propelled micromotors were investigated in solution systems containing gradient concentrations of H_2O_2 (0.50, 0.75, 1.00, 1.50, 2.00 wt%) and 0.3 wt% SDS. Micromotors, SDS, and H_2O_2 were drop-cast onto microscope slides for observation after liquid stabilization. The speed was measured by analyzing the motion videos taken by the optical microscope, and the motion of the micromotor in emulsion was studied in the same way.

2.5. Demulsification Test

The demulsification performance of the FPMs was evaluated by measuring transmittance changes of emulsions before and after treatment. To evaluate demulsification performance, 15 mg micromotors were added to 9.5 mL stable oil-in-water emulsion, followed by the addition of 500 μL H_2O_2 (30 wt%) as fuel. The final micromotor dosage in emulsion was 1.5 mg/mL, with H_2O_2 dosage of 1.5 wt%. Demulsification efficiency (DE) was calculated based on the light transmittance of the emulsion before and after treatment according to the equation listed below:

$$DE(\%) = (\frac{T_e - T_0}{T_0}) \times 100\%$$

where T_0 and T_e represent the transmittance before and after demulsification, respectively. Measurements in triplicate were averaged to determine the demulsification efficiency.

3. Results and Discussion

3.1. Preparation and Characterization of FPMs

Bio-derived kapok fibers possessed a unique tubular microstructure, making them ideal natural templates for fabricating bubble-driven micromotors. The preparation process of FPMs was shown in Figure 1a. Fe_3O_4 and MnO_2 were sequentially integrated onto the kapok fiber surface to construct a dual-responsive system combining magnetic steering and catalytic propulsion. Fe_3O_4 endowed the micromotors with magnetic responsiveness for facile recovery, while MnO_2 catalyzed H_2O_2 decomposition to generate bubble-driven autonomous motion. The self-propelled behavior enhanced contact with dispersed oil droplets and promoted active demulsification. In addition, a polydopamine interlayer was introduced for subsequent fluorinated thiol grafting, thereby tailoring the surface wettability of the micromotors toward hydrophobicity. The synergistic integration of catalytic bubble propulsion, magnetic recyclability, and surface hydrophobization enabled efficient interaction with oil droplets and subsequent oil-water separation.

SEM images revealed that the raw kapok fibers possessed a hollow tubular architecture with a smooth external surface (Figure 1b). After functionalization toward hydrophobicity, the resulting micromotors retained the original tubular morphology, while exhibiting a markedly roughened surface due to the deposition of PDA, MnO_2, and Fe_3O_4 nanoparticles (Figure 1c). High-magnification SEM images further demonstrated that MnO_2 and Fe_3O_4 nanoparticles were uniformly immobilized on the PDA-coated fiber surface (Figure 1d), indicating successful surface functionalization. In addition, EDS elemental mapping confirmed the homogeneous distribution of O, F, Mn, and Fe throughout the micromotor surface (Figure 1e), further verifying the successful incorporation of fluorinated groups and functional nanoparticles. As shown in Figure 2a, the prepared micromotors mainly

exhibited lengths ranging from 100 to 200 μm, suggesting a relatively uniform size distribution. These results collectively demonstrated that the proposed fabrication strategy enabled the successful construction of FPMs.

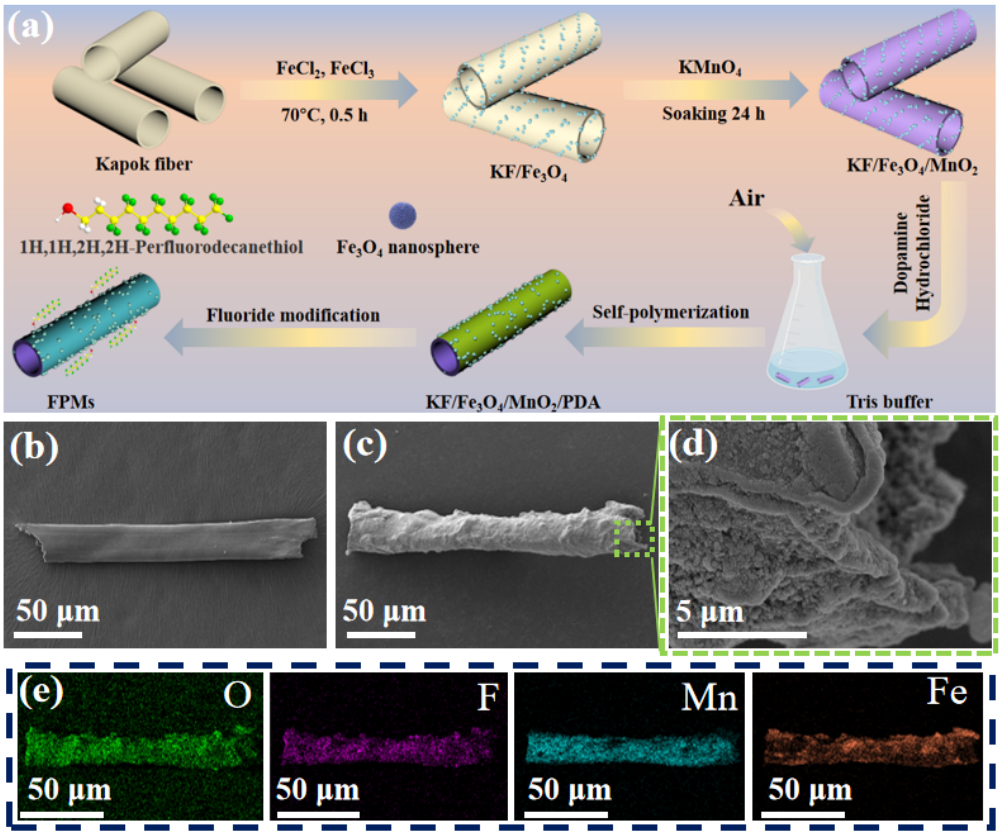

Figure 1. (**a**) Synthetic route of FPMs. SEM images of (**b**) raw kapok fibers and FPMs at (**c**) low and (**d**) high magnifications. (**e**) EDS elemental mapping of FPMs.

FTIR spectroscopy was employed to investigate the surface chemical changes during the modification process of the micromotors (Figure 2b). Raw kapok fibers exhibited characteristic absorption bands at approximately 3400 cm^{-1} and 1600 cm^{-1}, corresponding to O−H stretching and asymmetric −COO− stretching vibrations [32], respectively. After perfluoroalkyl modification, the FPMs displayed a distinct C−F stretching vibration band near 1200 cm^{-1}, confirming the successful grafting of perfluoroalkyl chains onto the fiber surface [33]. Meanwhile, the marked attenuation of the C−H stretching peak at around 2900 cm^{-1} indicated the replacement of original surface organic groups by the introduced fluorinated chains. These results demonstrated that the multistep modification strategy successfully introduced fluorinated functional groups onto the kapok fiber surface.

The crystalline structures of Fe_3O_4@KF, MnO_2@Fe_3O_4@KF, and FPMs were characterized by XRD (Figure 2c). The diffraction peaks at 30.1°, 35.4°, 43.1°, 57.0°, and 62.6° corresponded to the (2 0 0), (3 1 1), (4 0 0), (5 1 1), and (4 4 0) crystal planes of Fe_3O_4 (JCPDS No. 89-0691) [34]. In addition, diffraction peaks at 19.03°, 22.08°, 27.66°, and 38.69° corresponded to the (2 0 0), (1 1 0), (2 1 0), and (1 1 1) planes of MnO_2 (JCPDS No. 72-1983) [35]. These results confirmed the successful incorporation of Fe_3O_4 and MnO_2 into the kapok fiber-based micromotor structure. The magnetic properties of the FPMs were further evaluated by vibrating sample magnetometry (VSM) (Figure 2d). The micromotors exhibited a saturation magnetization value of 9.73 emu/g, indicating good magnetic responsiveness derived from the Fe_3O_4 component. Such magnetic responsiveness enabled the rapid magnetic recovery and manipulation of the micromotors under an external magnetic field, thereby facilitating the recycle of materials and minimizing the risk of secondary pollution.

X-ray photoelectron spectroscopy (XPS) was employed to investigate the surface chemical composition and elemental states of the FPMs. As shown in the survey spectrum (Figure 3a), the material surface mainly contained C, N, O, F, and Mn, confirming the successful incorporation of MnO_2 nanoparticles, PDA, and fluorinated thiol molecules through the multistep surface functionalization process. In the high-resolution C 1s spectrum (Figure 3b), the peaks centered at 284.80, 287.81, 290.76, and 293.10 eV were assigned to C−C/C−H, C−O, O−C=O, and $-CF_2-$ groups [36], respectively. The N 1s spectrum (Figure 3c) exhibited a characteristic peak at 399.74 eV, corresponding to pyrrolic or amino nitrogen species derived from the PDA coating. The O 1s spectrum (Figure 3d)

was deconvoluted into three components located at 530.45, 531.36, and 532.38 eV, corresponding to metal-oxygen bonds (Mn−O/Fe−O), C=O, and C−O groups [35]. Furthermore, the F 1s peak at 688.19 eV (Figure 3e) confirmed the successful grafting of the perfluoroalkyl chains [37]. The appearance of the $-CF_2-$ signal provided direct evidence for the successful introduction of fluorinated alkyl chains, which contributed to the formation of a low-surface-energy interface [38]. while the Mn 2p spectrum (Figure 3f) exhibited characteristic spin-orbit doublets at 641.48 and 653.23 eV, which were assigned to Mn $2p_{3/2}$ and Mn $2p_{1/2}$ of MnO_2 [39]. The observed spin–orbit splitting of approximately 11.8 eV confirmed that Mn was predominantly in the +4 oxidation state. Collectively, the XPS results demonstrated the successful construction of the micromotors integrating catalytic, magnetic, and hydrophobic functionalities.

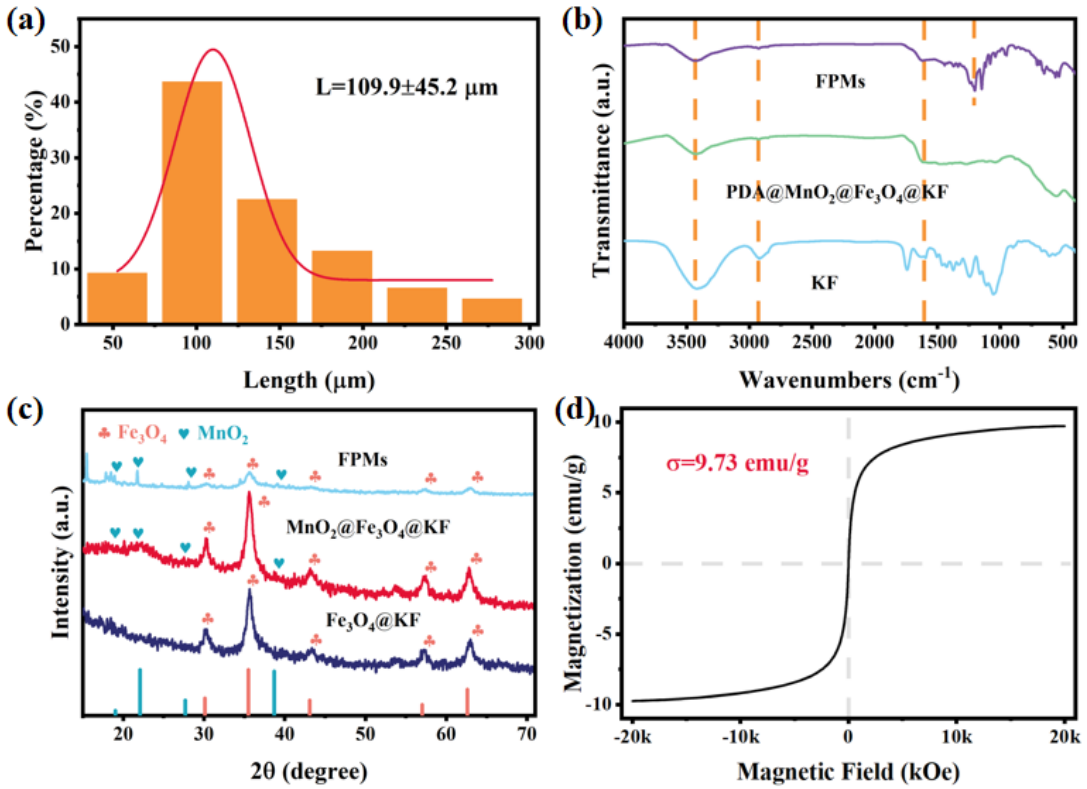

Figure 2. (**a**) Length distribution histogram of FPMs. (**b**) FT-IR spectra of kapok fibers, PDA@MnO_2@Fe_3O_4@KF, and FPMs. (**c**) XRD patterns of Fe_3O_4@KF, MnO_2@Fe_3O_4@KF, and FPMs. (**d**) Room-temperature magnetic hysteresis loop of FPMs.

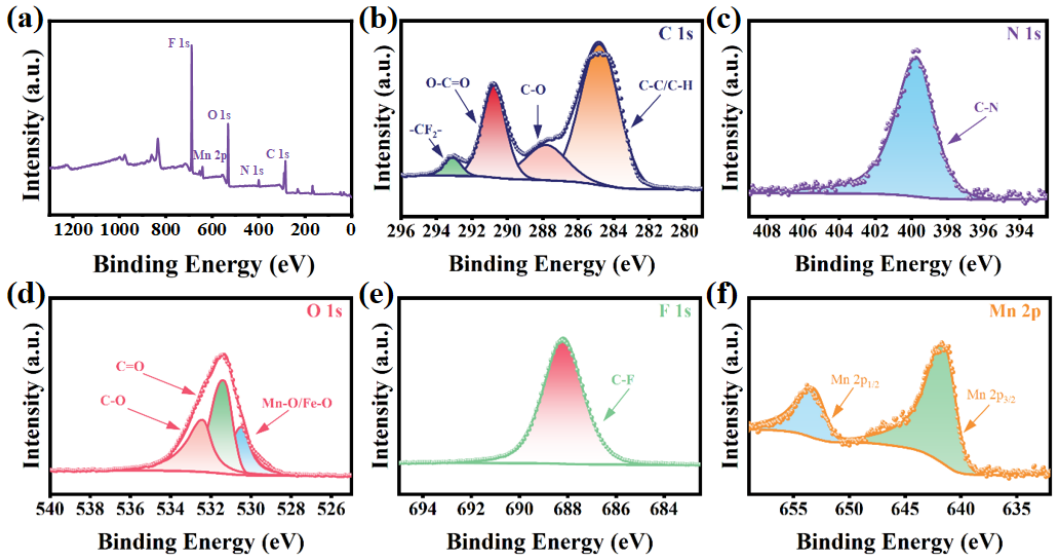

Figure 3. (**a**) XPS survey scan spectra of FPMs. The high resolution XPS spectra of (**b**) C 1s, (**c**) N 1s, (**d**) O 1s, (**e**) F 1s, and (**f**) Mn 2p.

The surface wettability evolution during the modification process was evaluated by water contact angle (WCA) measurements (Figure 4a–c). Raw kapok fibers exhibited a water contact angle of 130.7°, which was attributed to the presence of the natural wax layer on the fiber surface, indicating intrinsic hydrophobicity. After the sequential deposition of Fe_3O_4, MnO_2, and PDA, the water contact angle of the intermediate material dramatically decreased to 25.7°, suggesting that the introduction of hydrophilic metal oxides and PDA functional groups significantly enhanced surface hydrophilicity. Following fluorinated thiol grafting, the resulting FPMs exhibited a water contact angle of 123.6°, indicating the hydrophobic nature after surface fluorination. This wettability transition was mainly attributed to the introduction of low-surface-energy perfluoroalkyl chains onto the micromotor surface. The wettability transition of the micromotor surface was further evaluated using formamide. As shown in Figure 4d,e, the formamide contact angle increased markedly from 19.4° for PDA@MnO_2@Fe_3O_4@KF to 99.1° after fluorinated modification, indicating a substantial reduction in surface polarity. This reduction in surface polarity altered the wetting behavior of the micromotors and played an indispensable role in the demulsification process. The fluorinated surface provided favorable surface properties for efficient interaction with emulsified oil droplets during the demulsification process.

The interfacial distribution behaviors of PDA@MnO_2@Fe_3O_4@KF and FPMs were further evaluated in a petroleum ether (PE)/water biphasic system. After vigorous mixing, the phase distribution states of the materials were recorded after standing for 1 and 5 min (Figure 4f,g). PDA@MnO_2@Fe_3O_4@KF was mainly dispersed in the aqueous phase and gradually settled to the bottom of the container, indicating its relatively hydrophilic surface characteristics. In contrast, the FPMs rapidly migrated to and remained stably localized at the oil-water interface. This distinct interfacial behavior could be attributed to the enhanced hydrophobicity induced by fluorinated modification.

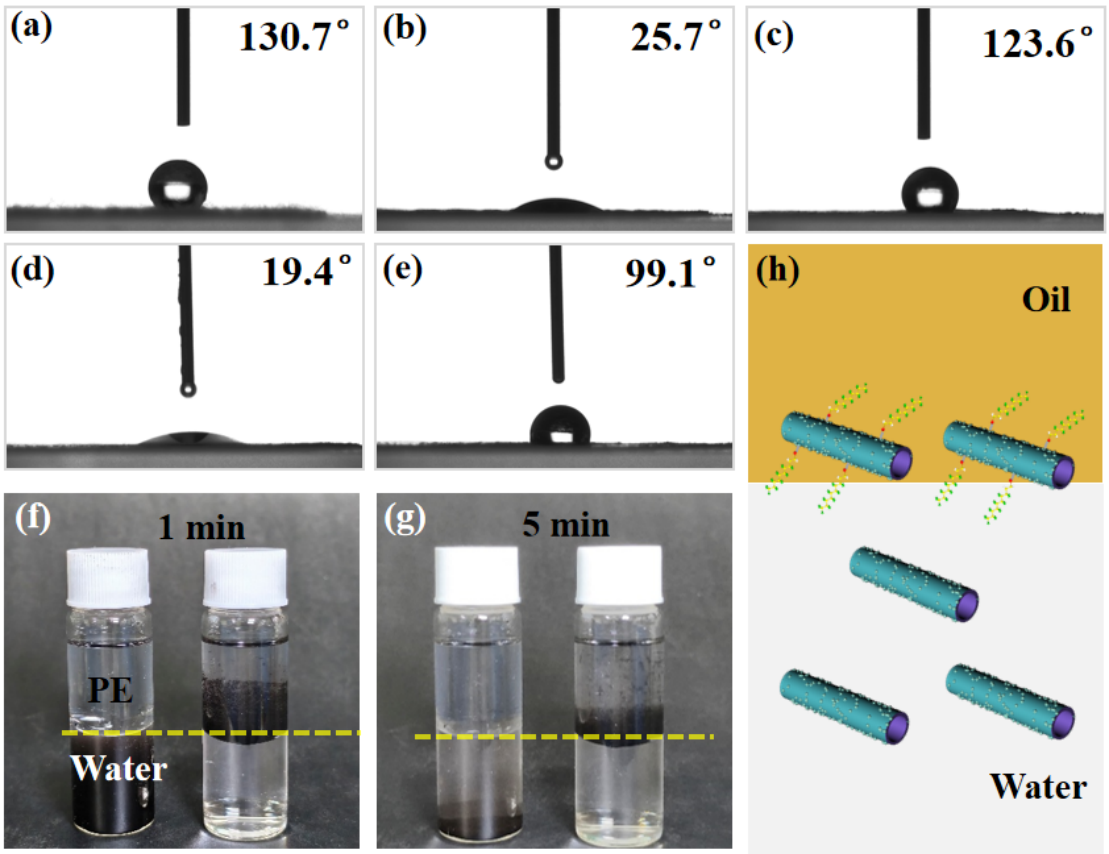

Figure 4. Water contact angles of (**a**) KF, (**b**) PDA@MnO_2@Fe_3O_4@KF, and (**c**) FPMs. Formamide contact angles of (**d**) PDA@MnO_2@Fe_3O_4@KF and (**e**) FPMs. Distribution photos of samples in the oil/water system after (**f**) 1 min and (**g**) 5 min (left: PDA@MnO_2@Fe_3O_4@KF, right: FPMs). (**h**) Schematic diagram of material distribution.

The surface charge evolution of the micromotors during the modification process was investigated by Zeta potential measurements (Figure 5a). At pH 7, raw kapok fibers exhibited a negative surface potential of −23.0 mV, which was mainly attributed to the presence of oxygen-containing functional groups on the fiber surface [40]. After Fe_3O_4 deposition, the Zeta potential shifted to 11.6 mV, indicating that the surface charge reversal was attributed to the strong positive charge of the introduced Fe_3O_4 nanoparticles. Following MnO_2 loading, the surface potential decreased markedly to −29.1 mV, suggesting the successful incorporation of negatively charged MnO_2 species.

Subsequent PDA coating partially neutralized the surface charge, resulting in a Zeta potential of −20.1 mV. The pH-dependent Zeta potential behavior of FPMs was presented in Figure 5b. As the solution pH increased, the Zeta potential gradually shifted toward more negative values, which could be attributed to the progressive deprotonation of surface functional groups under alkaline conditions. Such surface charge evolution could significantly influence interfacial interactions between the micromotors and emulsified oil droplets, thereby affecting the demulsification behavior of the system.

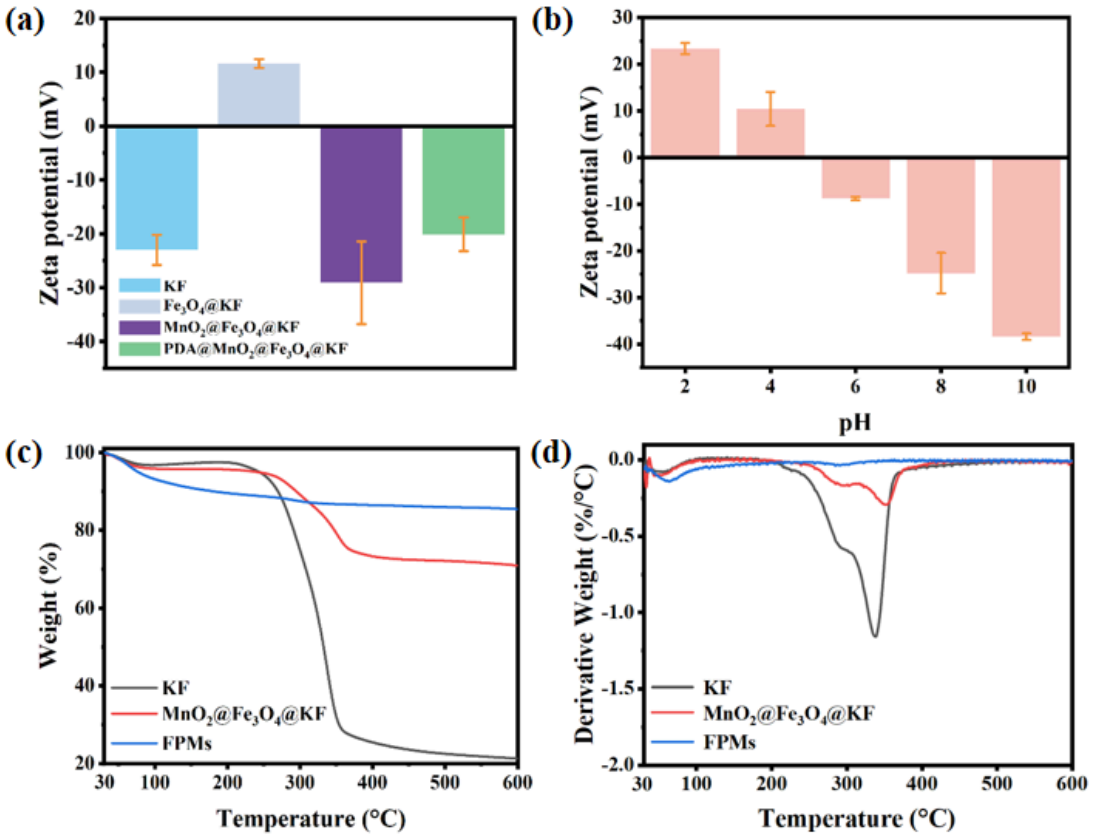

Figure 5. (**a**) Zeta potentials of KF, Fe_3O_4@KF, MnO_2@Fe_3O_4@KF, and PDA@MnO_2@Fe_3O_4@KF at pH 7, and (**b**) Zeta potential variations of FPMs at different pH values; (**c**) TG curves and (**d**) corresponding DTG curves of KF, MnO_2@Fe_3O_4@KF, and PDA@MnO_2@Fe_3O_4@KF.

Thermogravimetric (TGA) analysis was performed on samples at various stages under a nitrogen atmosphere, as shown in Figure 5c,d. The kapok fiber had a residual mass of 21.34% at 600 °C, while the MnO_2@Fe_3O_4@KF exhibited a residual mass of 70.93%, owing to the immobilization of metal oxides on the surface of kapok fibers. After modification with PDA and fluorinated thiol, the prepared FPMs retained 85.48% of its mass at 600 °C, exhibiting improved thermal stability. As revealed by the DTG curves (Figure 5d), the main thermal decomposition peak of raw kapok fibers appeared at approximately 338 °C, accompanied by a shoulder peak within the range of 288–307 °C, which was likely associated with the decomposition of hemicellulose and surface organic components [41,42]. After loading with Fe_3O_4 and MnO_2, the main decomposition peak of MnO_2@Fe_3O_4@KF shifted to 353 °C. In contrast, the decomposition rate of FPMs was relatively gradual and stable over the range of 30–600 °C. These results demonstrated that the incorporation of Fe_3O_4, MnO_2, PDA, and fluorinated functional groups significantly altered the surface physicochemical properties of the kapok fibers.

3.2. Motion Study of Micromotors

The propulsion behavior of the fabricated micromotors was investigated using optical microscopy. In the presence of H_2O_2, MnO_2 nanoparticles on the micromotor surface catalyzed the decomposition of H_2O_2 to generate O_2 bubbles, thereby producing bubble-driven self-propulsion. As shown in Figure 6a, the micromotors exhibited longer motion trajectories with increasing H_2O_2 concentration over a 5 s observation period. Correspondingly, the average propulsion velocity increased from 26.74 μm/s to 124.14 μm/s as the H_2O_2 concentration increased from 0.50 wt% to 2.00 wt% (Figure 6b), indicating that the propulsion performance of the micromotors could be effectively regulated through fuel concentration. Time-lapse optical images further demonstrated that the

micromotors maintained stable locomotion behavior both in pure aqueous solution and in surfactant-stabilized emulsions containing 1.00 wt% H_2O_2 (Figure 6c, d and Videos S1 and S2). Such autonomous motion was expected to enhance mass transfer and convection, thereby increasing contact frequency between the micromotors and dispersed oil droplets during the demulsification process. In addition, owing to the incorporation of Fe_3O_4 nanoparticles, the micromotors exhibited magnetic responsiveness and could be directionally manipulated under an external magnetic field. As shown in Figure 6e, the micromotors achieved magnetically guided motion along a predetermined trajectory, enabling targeted implement of demulsification tasks. The combination of autonomous propulsion and magnetic guidance provided the micromotors with excellent maneuverability for active oil-droplet interaction and controllable demulsification.

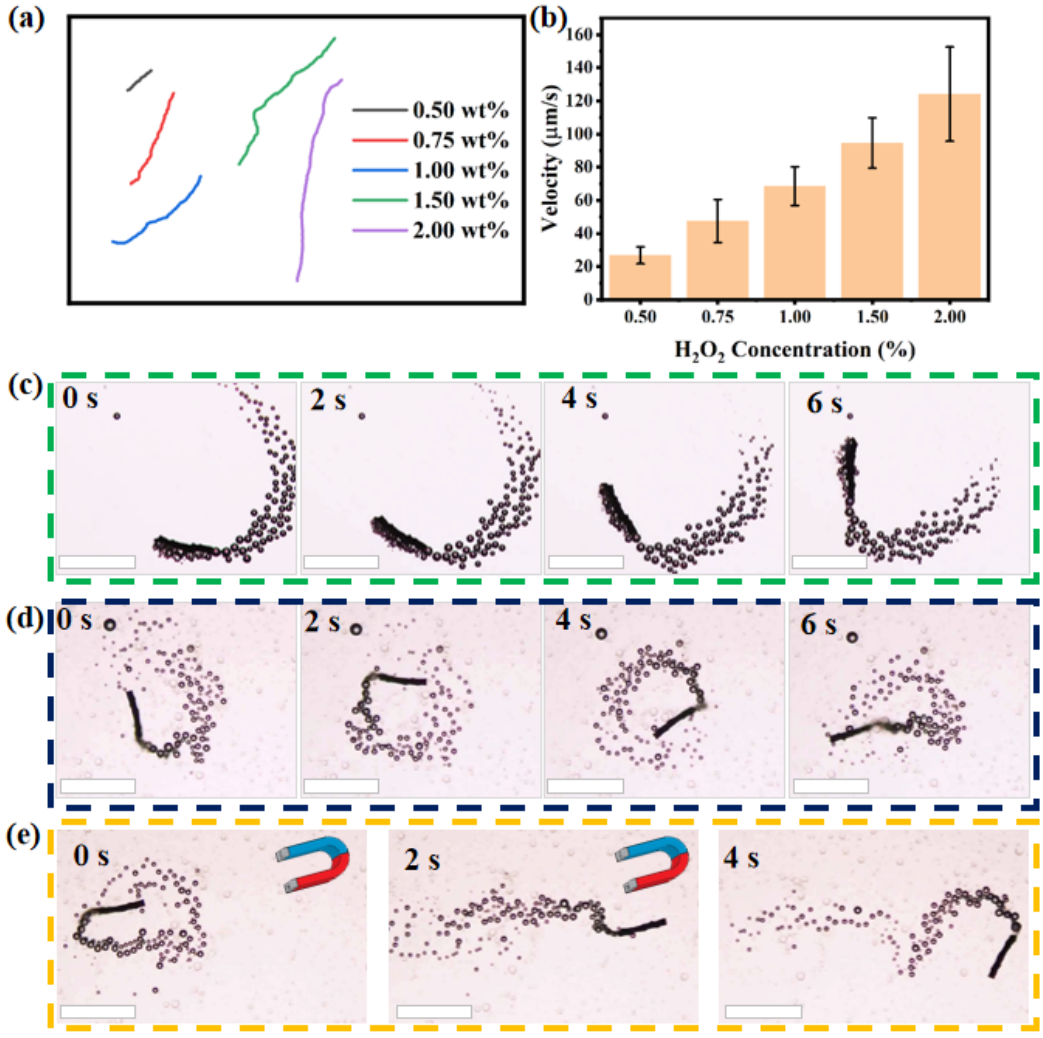

Figure 6. (**a**) Motion trajectories of FPMs in H_2O_2 solutions with different concentrations within 5 s. (**b**) Average velocities of micromotors in different concentrations of H_2O_2 (data derived from 10 independent experiments). Time-lapse images of micromotors in (**c**) water and (**d**) emulsion with 1.00 wt% H_2O_2. (**e**) Time-lapse images of micromotor motion in emulsion under magnetic field guidance. The concentration of SDS is 0.3 wt%, and the scale bars are 200 μm.

3.3. Demulsification Performance of Micromotors

The demulsification performance of the micromotors as active heterogeneous demulsifiers was evaluated by comparing the self-propelled system (in the presence of H_2O_2) with a static control system (without H_2O_2). Upon introduction into the emulsion, the self-propelled micromotors rapidly generated O_2 bubbles through catalytic decomposition of H_2O_2, producing continuous bubble-driven motion within the emulsion system. The interaction of micromotors with the oil droplets together with the function of generated bubbles promoted the upward transport of oil droplets and facilitated the formation of an oil layer at the liquid surface (Figure 7a). In contrast, the static micromotors in the control group rapidly settled to the bottom of the container and exhibited limited interfacial interaction with dispersed oil droplets (Figure 7a). Visual observations revealed that the emulsion in the control

system remained stable throughout the experimental period, whereas the self-propelled micromotors effectively destabilized the emulsion and induced rapid phase separation [43]. Within 27 min, the emulsion transformed from a milky and turbid state into a clarified solution. The enhanced demulsification behavior could be attributed to the autonomous motion of micromotors and the function of simultaneously generated bubbles. The induced active transport behavior accelerated oil droplet aggregation and coalescence, thereby promoting efficient oil-water separation. To decouple the contributions of bubble-driven motion and surface functionalization, control experiments was performed under identical conditions (pH 7, 45 °C, 1.5 wt% H_2O_2, 27 min), and the results were summarized in Figure S1. The H_2O_2-alone system achieved a demulsification efficiency of only 21.27%, which may arise from mild oxidative degradation of the surfactant film and weak spontaneous bubble flotation. Non-fluorinated micromotors (PDA@MnO_2@Fe_3O_4@KF) under self-propelled conditions gave an efficiency of 49.63%. In contrast, the FPMs achieved an efficiency of 98.19% and the dramatic improvement was attributed to the low-surface-energy fluorinated coating. Collectively, these control experiments demonstrate that the demulsification mechanism involves both bubble-driven flotation and surface energy-driven coalescence.

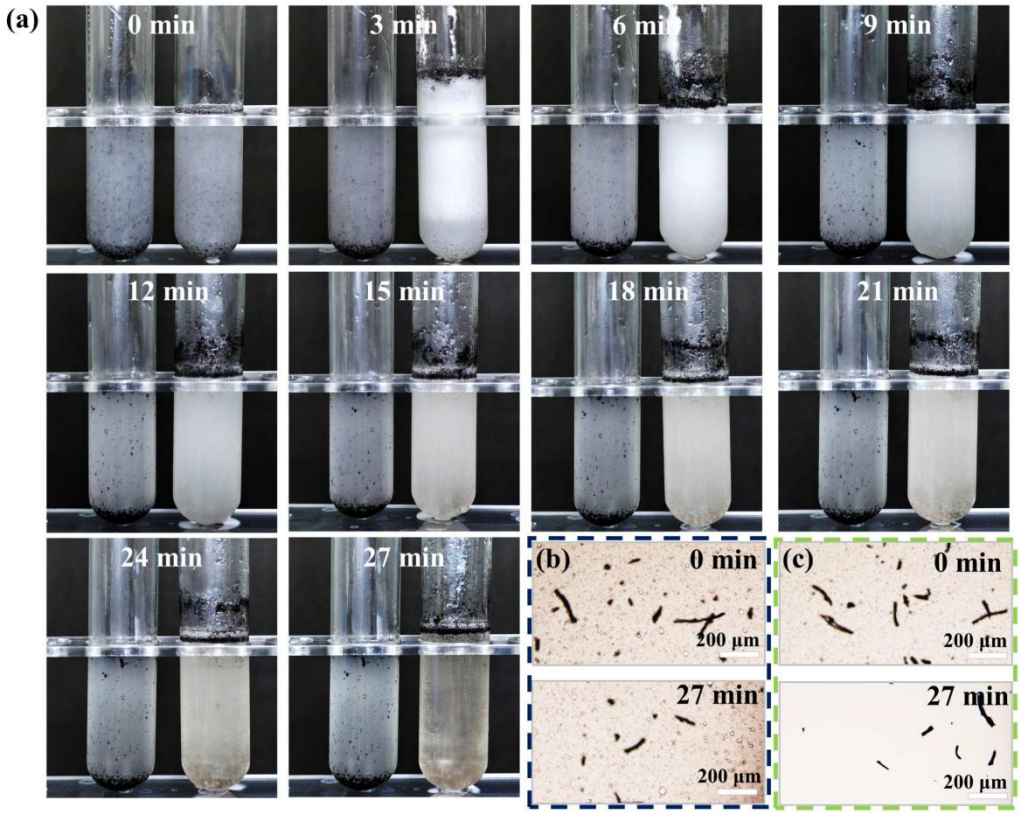

Figure 7. (**a**) Time-lapse images of the demulsification process by static micromotors (without H_2O_2, left) and moving micromotors (right) over 27 min. (**b**,**c**) Microscopic images of the emulsion for static (without H_2O_2) and moving micromotors at 0 and 27 min, respectively. All scale bars are 200 μm.

Optical microscopy was further employed to evaluate the residual oil droplets in the emulsions after 27 min of treatment. As shown in the microscopic images, the control group still contained a large population of finely dispersed oil droplets, and no apparent phase separation was observed at the macroscopic level (Figure 7b). In contrast, the emulsion treated with self-propelled micromotors exhibited a substantial reduction in residual oil droplets, with the lower aqueous phase appearing nearly free of dispersed oil (Figure 7c). These observations suggested that the self-propelled micromotors effectively accelerated emulsion destabilization through autonomous locomotion and bubble-assisted flotation effects.

3.4. Influence Factors of Demulsification Performance

To further investigate the practical application potential of FPMs in the treatment of emulsified wastewater, the demulsification conditions for the micromotors were optimized. The demulsification efficiency was quantitatively evaluated by measuring changes in light transmittance before and after treatment of the emulsion. Specifically, with the H_2O_2 concentration fixed at 1.5 wt%, the effects of temperature, pH, and micromotor dosage

on demulsification efficiency were investigated. Figure 8a showed the effect of temperature on demulsification efficiency at a micromotor dosage of 1.5 mg/mL and pH 7. As the temperature rose from 25 °C to 65 °C, the demulsification efficiency increased from 61.30% to 98.19% at 45 °C, and then declined to 63.78% at 65 °C. The decline in demulsification efficiency at high temperatures may be attributed to the thermal decomposition of the H_2O_2 fuel. As shown in Figure 8b, the effect of pH on demulsification efficiency was investigated under fixed conditions of 45 °C and a micromotor dosage of 1.5 mg/mL. Under acidic conditions from pH 1 to 4, the demulsification efficiency increased from 77.63% to 88.28%. At pH 7, the highest demulsification efficiency of 98.19% was achieved. As the pH increased from 7 to 13, the demulsification efficiency decreased slightly but remained above 90%. These results indicated that the FPMs exhibited stable demulsifying performance under neutral and alkaline conditions. Figure 8c showed the effect of micromotor dosage on demulsification efficiency at pH 7 and 45 °C. Within the dosage range of 0.5–2.5 mg/mL, the demulsification efficiency increased significantly with increasing micromotor dosage. When the dosage was raised from 0.5 mg/mL to 1.5 mg/mL, the efficiency rose from 75.04% to 98.19% and further increase of the dosage to 2.5 mg/mL yielded no significant improvement. In summary, the system achieved optimal demulsification efficiency at pH 7, 45 °C, and a micromotor dosage of 1.5 mg/mL.

In addition to optimizing the influence parameters, the stability and reusability of the FPMs were evaluated under the optimal conditions. As shown in Figure S3, the demulsification efficiency was 98.41% in the first cycle, and it remained at 98.10% after the second cycle. With further reuse, the efficiency slightly decreased to 97.13% in the third cycle and 94.38% in the fourth cycle. These results demonstrated that the FPMs exhibit good stability and reusability over four consecutive cycles. Beyond the reusability, the environmental friendliness of the FPMs was further evaluated by quantifying the leaching of potentially hazardous elements into the treated water after four consecutive cycles using inductively coupled plasma optical emission spectrometry (ICP-OES). It should be noted that since fluorine cannot be reliably quantified due to its high ionization potential, we used total sulfur (S) concentration as an indirect indicator of fluorinated thiol release. As shown in Table S1, the concentrations of Fe, Mn, and S in the final aqueous phase were determined to be 0.0079 mg/L, 1.5040 mg/L, and 0.2410 mg/L, respectively, which were all below the wastewater discharge standard. Collectively, the ICP-OES results, together with the sustained demulsification efficiency over multiple cycles highlight their potential for practical wastewater treatment.

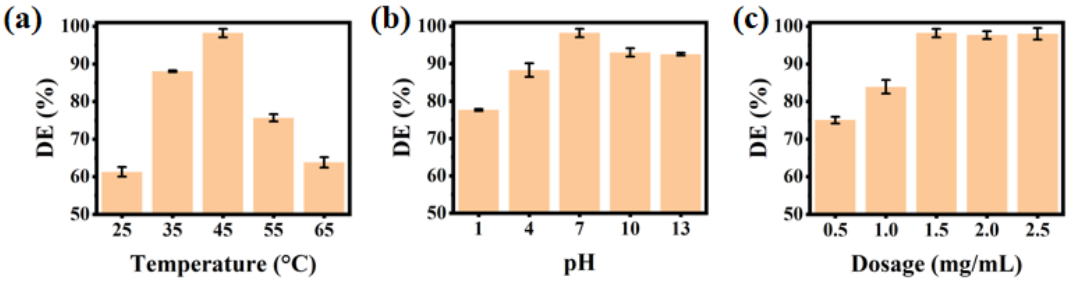

Figure 8. Effects of (**a**) temperature, (**b**) pH, and (**c**) micromotor dosage on the demulsification efficiency of FPMs.

4. Conclusions

In this study, bio-derived tubular micromotors were successfully fabricated using natural hollow kapok fibers as a biotemplate for efficient demulsification of oil-in-water emulsion wastewater. The synthesis strategy utilized readily available and environmentally benign raw materials, along with a simple and scalable preparation process, demonstrating good potential for practical applications. Compared with conventional static demulsification materials, the prepared FPMs exhibited significantly enhanced demulsification performance owing to their active bubble propulsion. The autonomous propulsion and bubble-induced mass transfer significantly accelerated oil droplet aggregation and coalescence. Meanwhile, the buoyancy effect generated by catalytic bubbles promoted the upward transport and enrichment of oil droplets at the liquid surface, thereby accelerating phase separation. Demulsification experiments demonstrated that the FPMs maintained excellent separation performance across a broad pH range from neutral to alkaline. Under optimized operating conditions, the maximum demulsification efficiency of the prepared micromotors reached 98.19% within 27 min. This study offers new insights into oily emulsion wastewater treatment via the design of bio-derived active demulsifiers.

Supplementary Materials

The additional data and information can be downloaded at: https://media.sciltp.com/articles/others/26081116 29221017/RE-26060029-SI.pdf. Text S1. Detailed information of materials and related characterization apparatus. Figure S1. Demulsification efficiencies of different control systems (non-fluorinated motors + H_2O_2, FPMs + H_2O_2). Figure S2. Repeated demulsification experiments of FPMS. Table S1. ICP-OES analysis of treated water. Video S1. The random self-propulsion of FPMs in the solution contained 1.0 wt% H_2O_2 and 0.3 wt% SDS. Video S2. The random self-propulsion of FPMs in the O/W emulsion contained 1.0 wt% H_2O_2 and 0.3 wt% SDS.

Author Contributions

Z.W.: Writing—original draft, visualization, methodology, investigation, formal analysis, data curation. M.T.: Methodology, investigation, formal analysis, validation, supervision. H.W.: Writing—review & editing, supervision, project administration, funding acquisition, conceptualization. All authors have read and agreed to the published version of the manuscript.

Funding

This work was financially supported by National Natural Science Foundation of China (52575678), the interdisciplinary program of science and engineering from China University of Mining and Technology.

Institutional Review Board Statement

Not applicable.

Informed Consent Statement

Not applicable.

Data Availability Statement

The raw data used in this study are available upon reasonable request from the authors. The authors will ensure that qualified professionals have access to these data for at least 10 years after the publication of this paper.

Conflicts of Interest

The authors declare no conflict of interest.

Use of AI and AI-Assisted Technologies

No AI tools were utilized for this paper.

References

1. Gao, H.; Qian, H.; Meng, Z.; et al. Biomimetic materials for efficient emulsion separation: Based on the perspective of energy. *Adv. Colloid Interface Sci.* **2025**, *341*, 103486.
2. Lei, J.; Qi, R.; Yang, Y.; et al. Targeted stepwise pre-adsorption for enhanced nanofiltration removal of dissolved organic pollutants in petrochemical wastewater. *Water Res.* **2025**, *287*, 124390.
3. Chen, J.; Chen, J.; Zheng, L.; et al. Cellulose-based aerogels for efficient dye sorption and oil-water separation in textile wastewater treatment. *Int. J. Biol. Macromol.* **2025**, *310*, 143612.
4. Bai, R.; Huang, Y.; Zhang, Q.; et al. Nacre-inspired mineral-hydrogel PVDF membrane with superhydrophilicity, antifouling and antimicrobial properties for food oily wastewater treatment. *J. Hazard. Mater.* **2026**, *504*, 141340.
5. Gondikas, A.; Mattsson, K.; Hassellöv, M. A new form of hazardous microparticulate contamination to the marine environment from ships using heavy fuel oil with exhaust gas scrubbers—Characterization and implications for fate, transport and ecotoxicity. *Sci. Total Environ.* **2025**, *959*, 178263.
6. Liu, Z.; Chen, M.; Lin, C.; et al. Solar-assisted high-efficient cleanup of viscous crude oil spill using an ink-modified plant fiber sponge. *J. Hazard. Mater.* **2022**, *432*, 128740.
7. Al Zarkani, H.; El-Fadel, M. Can integrating life cycle assessment with optimization modeling identify strategies for produced water reuse in offshore oilfield explorations and production? Model development and testing. *Environ. Impact Assess. Rev.* **2026**, *116*, 108097.

8. Chen, G.; Yuan, M.; Xiao, Y.; et al. Integrated physiological characteristics and temporal transcriptomic analysis reveal the molecular mechanism of Pseudomonas aeruginosa degrading diesel stimulated by extracellular metabolites of euglena. *Chem. Eng. J.* **2023**, *475*, 146507.
9. Hemati, S.; Heidari, M.; Momenbeik, F.; et al. Co-occurrence of polycyclic aromatic hydrocarbons and heavy metals in various environmental matrices of a chronic petroleum polluted region in Iran; Pollution characterization, and assessment of ecological and human health risks. *J. Hazard. Mater.* **2024**, *478*, 135504.
10. Faisal, W.; Almomani, F. A critical review of the development and demulsification processes applied for oil recovery from oil in water emulsions. *Chemosphere* **2021**, *291*, 133099.
11. Mazumder, A.; Das, S.; Sen, D.; et al. Kinetic analysis and parametric optimization for bioaugmentation of oil from oily wastewater with hydrocarbonoclastic Rhodococcus pyridinivorans F5 strain. *Environ. Technol. Innov.* **2020**, *17*, 100630.
12. Baig, U.; Faizan, M.; Sajid, M. Multifunctional membranes with super-wetting characteristics for oil-water separation and removal of hazardous environmental pollutants from water: A review. *Adv. Colloid Interface Sci.* **2020**, *285*, 102276.
13. Liu, B.; Chen, B.; Ling, J.; et al. Development of advanced oil/water separation technologies to enhance the effectiveness of mechanical oil recovery operations at sea: Potential and challenges. *J. Hazard. Mater.* **2022**, *437*, 129340.
14. Liao, J.; Li, B.; Ran, L.; et al. Application, challenges, and opportunities of organic metal frameworks materials in oil-water separation. *J. Environ. Chem. Eng.* **2025**, *13*, 119324.
15. Li, S.; Liu, Y.; Du, S.; et al. Photothermal-driven bio-based composite sponge for sustainable oil-water separation: A green strategy utilising vanillin-crosslinked chitosan. *Carbohydr. Polym.* **2026**, *380*, 125088.
16. Chen, S.; Zhao, Z.; Chen, C.; et al. 3D-printed super-wetting membranes with in situ grown MOF for efficient oil-water separation. *J. Hazard. Mater.* **2025**, *498*, 139821.
17. Jiang, S.; Niu, H.; Gu, X.; et al. Perfluoroalkyl functionalized superhydrophobic covalent organic frameworks for excellent oil–water membrane separation and anhydrous proton conduction. *Small* **2024**, *20*, 2403772.
18. Tanudjaja, H.; Hejase, C.; Tarabara, V.; et al. Membrane-based separation for oily wastewater: A practical perspective. *Water Res.* **2019**, *156*, 347–365.
19. Wang, K.; Ma, E.; Cui, H.; et al. Amphiphilic micromotors as active demulsifiers for rapid oil–water separation. *Appl. Surf. Sci.* **2023**, *640*, 158272.
20. Wang, L.; Villa, K. Self-propelled micro/nanomotors for removal of insoluble water contaminants: Microplastics and oil spills. *Environ. Sci. Nano* **2021**, *8*, 3440–3451.
21. Urso, M.; Ussia, M.; Pumera, M. Smart micro- and nanorobots for water purification. *Nat. Rev. Bioeng.* **2023**, *1*, 236–251.
22. Sun, X.; Yang, H.; Liang, Y.; et al. Light-propelled super-hydrophobic sponge motor and its application in oil–water separation. *ACS Appl. Mater. Interfaces* **2023**, *15*, 43205–43215.
23. Lin, J.; Zhou, W.; Wu, Q.; et al. Shape, morphology, and components-dependent motion and water purification performance study of multi-metal–organic frameworks based micromotors. *Sep. Purif. Technol.* **2025**, *362*, 131559.
24. Tan, M.; Shi, C.; Cui, C.; et al. Efficient demulsification of oil-in-water emulsion triggered by pollen-based micromotors. *Colloids Surf. A Physicochem. Eng. Asp.* **2025**, *733*, 139355.
25. Hou, J.; Liu, H.; Huang, L.; et al. Recent advances in micro/nano-robots for environmental pollutant removal: Mechanism, application, and prospect. *Chem. Eng. J.* **2024**, *498*, 155135.
26. Minh, T.; Ncibi, M.; Srivastava, V.; et al. Micro/nano-machines for spilled-oil cleanup and recovery: A review. *Chemosphere* **2021**, *271*, 129516.
27. Jiang, Y.; An, J.; Zhai, S.; et al. Research progress on biomass-based materials for oil/water separation: Designing strategy and efficiency mechanism. *Int. J. Biol. Macromol.* **2024**, *283*, 137646.
28. Jin, R.; Gong, J.; Xiang, B.; et al. Biomass materials with special wettability: A sustainable solution for efficient oil–water separation. *J. Mater. Chem. A* **2024**, *12*, 23315–23336.
29. He, Y.; Guo, Z. Natural polymers-based separation membrane for high-efficient separation of oil water mixture. *Nano Today* **2024**, *57*, 102367.
30. Wang, Y.; Lu, H.; Wang, X.; et al. Green tubular micro/nano architecture constructed by in-situ planting of small AgNPs on Kapok fiber for oil spill recovery, smart oil–water separation and multifunctional applications. *Sep. Purif. Technol.* **2023**, *311*, 123278.
31. Liu, W.; Xu, J.; Sun, Q.; et al. Mechanically robust, flame-retardant, and waterproof kapok fiber/sodium alginate composite aerogel for building thermal insulation. *Int. J. Biol. Macromol.* **2025**, *318*, 144842.
32. Takahashi, K.; Nakagawa, Y.; Sato, Y.; et al. pH-responsive release of anesthetic lidocaine derivative QX-OH from mesoporous silica nanoparticles mediated by ester bonds. *J. Drug Deliv. Sci. Technol.* **2022**, *78*, 103977.
33. Chen, L.; Li, L.; Zhao, X.; et al. Construction of antifouling fluorinated polymer brush via activators regenerated by electron transfer ATRP and thiol-epoxy click reaction. *React. Funct. Polym.* **2021**, *165*, 104974.
34. Fu, X.; Sarker, S.; Ma, W.; et al. Novel phenylalanine-modified magnetic ferroferric oxide nanoparticles for ciprofloxacin removal from aqueous solution. *J. Colloid Interface Sci.* **2022**, *632*, 345–356.

35. Shi, C.; Wang, K.; Cui, H.; et al. Bio-templated micromotors for simultaneous adsorption and degradation of microplastics. *Surf. Interfaces* **2024**, *54*, 105144.
36. Morgan, D. Comments on the XPS analysis of carbon materials. *C* **2021**, *7*, 51.
37. Chen, C.; Levitin, G.; Hess, D.; et al. XPS investigation of Nafion® membrane degradation. *J. Power Sources* **2007**, *169*, 288–295.
38. Ghorabi, S.; Ashtiani, F.; Karimi, M.; et al. Development of a novel dual-bioinspired method for synthesis of a hydrophobic/hydrophilic polyethersulfone coated membrane for membrane distillation. *Desalination* **2021**, *517*, 115242.
39. Chu, J.; Wu, Y.; Zhang, H.; et al. Self-propelled MnO_2@$MnIn_2S_4$@coal gangue micromotor as high-performance photo-Fenton catalyst for enhanced synergetic degradation of xanthate. *J. Environ. Chem. Eng.* **2024**, *12*, 114599.
40. Baltazar-y-Jimenez, A.; Bismarck, A. Wetting behavior, moisture up-take and electrokinetic properties of lignocellulosic fibers. *Cellulose* **2006**, *14*, 115–127.
41. Kumar, R.; Hynes, N.; Senthamaraikannan, P.; et al. Physicochemical and thermal properties of ceiba pentandra bark fiber. *J. Nat. Fibers* **2017**, *15*, 822–829.
42. Kim, H.; Yu, S.; Kim, M.; et al. Progressive deconvolution of biomass thermogram to derive lignocellulosic composition and pyrolysis kinetics for parallel reaction model. *Energy* **2022**, *254*, 124446.
43. Zhou, J.; Zhang, X.; He, L.; et al. Nano-modification of carboxylated polyether for enhanced room temperature demulsification of oil-water emulsions: Synthesis, performance and mechanisms. *J. Hazard. Mater.* **2022**, *439*, 129654.